AIAA JOURNAL
Vol. 30, No. 4, April 1992

Structure of Supersonic Turbulent Flow Past a Swept Compression Corner

Doyle D. Knight*
Rutgers University, New Brunswick, New Jersey 08903
C. C. Horstman†
NASA Ames Research Center, Moffett Field, California 94035
and
Seymour Bogdonoff‡
Princeton University, Princeton, New Jersey 08544

The structure of the shock wave/turbulent boundary-layer interaction generated by a three-dimensional swept compression corner has been investigated through a combined experimental and theoretical research program. The flowfield geometry is defined by the streamwise compression angle α and the sweep angle λ of the corner. The present study examines two different configurations, namely, (α, λ) = (24 deg, 40 deg) and (24 deg, 60 deg) at Mach 3 and $Re_{\delta_\infty} \approx 9\times10^5$. The theoretical model is the three-dimensional Reynolds-averaged compressible Navier-Stokes equations with turbulence incorporated using a turbulent eddy viscosity. Four different turbulence models (Baldwin-Lomax, Cebeci-Smith, Jones-Launder with wall functions, and Jones-Launder integrated to the wall) were employed. The calculated flowfields display general agreement with experimental data for surface pressure and good agreement with experimental flowfield profiles of pitot pressure and yaw angle. The principal feature of the flowfield is a large vortical structure approximately aligned with the corner. The entrainment of incoming fluid into the vortical structure is strongly affected by the sweep angle λ. Viscous (turbulent and molecular) effects appear to be important only in the immediate vicinity of the surface and in an isolated region within the interaction and near the corner.

Introduction

THE interaction between shock waves and turbulent boundary layers is an important problem in modern fluid dynamics. Many practical applications in high-speed aerodynamics and propulsion evidence the phenomenon, and its understanding is, therefore, both relevant and important. Recent reviews[1,2] have described experimental and theoretical (computational and analytical) progress.

In a series of recent papers,[3-5] collaborative experimental and theoretical (computational) investigations of the three-dimensional single fin (Fig. 1) have been conducted at Mach 3. These previous studies focused on a range of inviscid shock strengths p_2/p_1 up to 3.7 (where p_2/p_1 is the inviscid shock pressure ratio) and Reynolds numbers Re_{δ_∞} from 2.5×10^5 to 9×10^5 where δ_∞ is the incoming boundary-layer thickness. The theoretical model was the three-dimensional compressible Reynolds-averaged Navier-Stokes equations with turbulence incorporated using a turbulent eddy viscosity. Several different zero- and two-equation turbulence models were examined. The theoretical predictions displayed general agreement with experimental data for surface pressure and good agreement with experimental boundary-layer profiles of pitot pressure, static pressure, and yaw angle. (Note that the exact extent of the boundary layer is not well defined for these three-dimensional interactions since the inviscid flow is nonuniform. Therefore, these boundary-layer profiles encompassed both the nominal boundary layer and the nonuniform inviscid flow.) The computed flowfields were found to be insensitive to the turbulence model employed except within a small fraction of the boundary layer adjacent to the surface where the computed profiles displayed modest differences among the predictions of the various turbulence models and experiment. The flowfield was observed to be dominated by a large vortex aligned approximately with the inviscid shock. More recent computations[6] at Mach 4 for shock strengths p_2/p_1 up to 5.1 displayed general agreement with experimental measurements of surface pressure and surface flow direction (i.e., the direction of the surface shear stress), but significantly underestimated the peak skin friction.

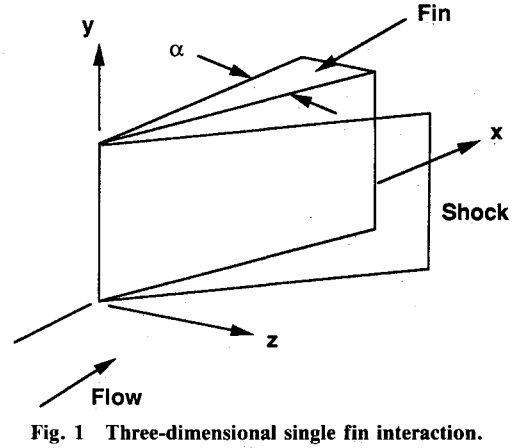

Fig. 1 Three-dimensional single fin interaction.

Received Feb. 5, 1991; revision received July 6, 1991; accepted for publication July 8, 1991.

*Professor, Department of Mechanical and Aerospace Engineering. Associate Fellow AIAA.
†Senior Scientist. Associate Fellow AIAA.
‡Professor Emeritus, Senior Research Scholar, Department of Aerospace and Mechanical Engineering. Fellow AIAA.

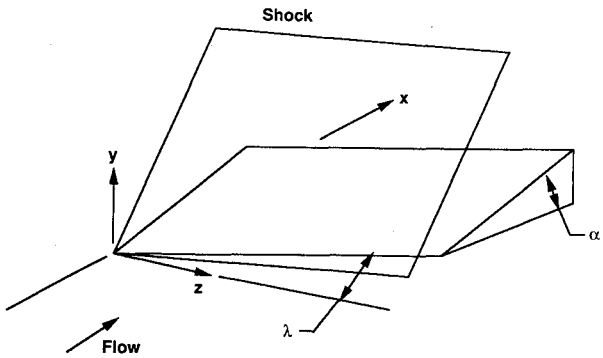

Fig. 2 Three-dimensional swept compression corner.

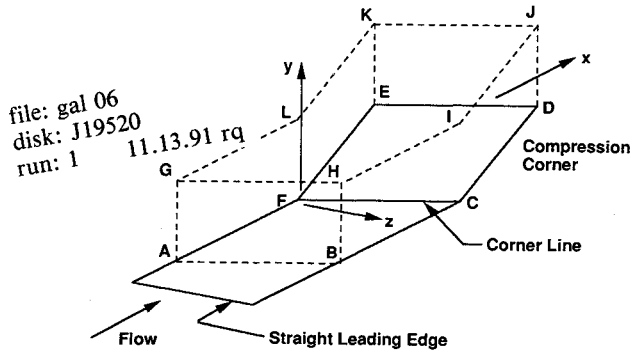

Fig. 3 Computational domain.

The present paper focuses on a collaborative experimental and theoretical (computational) investigation for the three-dimensional swept-compression corner shown in Fig. 2. The geometry is defined by the streamwise compression angle α, measured in a plane parallel to the upstream flow, and the sweep angle λ. The flowfield is defined by the freestream Mach number M_∞, Reynolds number Re_{δ_∞}, and wall temperature boundary conditions (e.g., adiabatic). The objectives of the present effort are to examine the efficacy of the theoretical models and to determine the flowfield structure. The efficacy of several zero- and two-equation turbulence models are examined through comparison with experimental data for surface pressure and boundary-layer profiles of pitot pressure and yaw angle. Grid refinement studies are performed to ascertain the accuracy of the numerical solutions. Provided that reasonable agreement is obtained between the computations and experiment, the calculated flowfields can be employed to determine the basic flowfield structure of the three-dimensional swept-compression corner and compared with the structure previously elucidated for the three-dimensional single fin.

Description of Experiments

The experiments were conducted in the high Reynolds number blowdown wind tunnel at the Princeton Gas Dynamics Laboratory. The experiments were conducted by various researchers and reported previously.[7-10] The present study focuses on two configurations, namely, $(\alpha, \lambda) = (24$ deg, 40 deg) and (24 deg, 60 deg), at Mach 2.95 for $Re_{\delta_\infty} \approx 9\times10^5$. A summary of the experimental test conditions is provided in Table 1. The incoming flow was an equilibrium, two-dimensional turbulent boundary layer that has been extensively surveyed[11,12] and observed to closely fit the law of the wall and wake.[13] The boundary-layer thickness for case B was determined by the first author using a fit of the experimental profile to the law of the wall and wake, and is 18% below the value reported by the experiment.[8] This discrepancy is attributable to the difference in the methods employed for determining δ_∞. Experimental data include surface pressure and flow direction (using the kerosene-lamp-black technique[1]), and pitot pressure p_p and yaw angle β profiles at several locations. The yaw angle $\beta = \tan^{-1}(w/u)$, where u and w are the velocity components in the x and z directions, respectively (see Fig. 2).

Table 1 Experimental conditions

Case	α, deg	λ, deg	δ_∞, cm	p_2/p_1	Re_{δ_∞}	Reference
A	24	60	1.3	3.3	8.7×10^5	9
B	24	40	1.3	4.0	8.1×10^5	8, 10

Table 2 Summary of computations

Case	α, deg	λ, deg	Re_{δ_∞}	Turbulence Model	δ_∞ on ABHG
1	24	60	8.9×10^5	Baldwin-Lomax	Variable
2	24	60	9.8×10^5	Jones-Launder (WF[a])	Variable
3	24	40	8.1×10^5	Cebeci-Smith	Constant
4	24	40	8.1×10^5	Jones-Launder	Constant
5	24	40	8.1×10^5	Baldwin-Lomax	Variable

[a]WF = use of wall functions.

Description of Computations

The theoretical model is the three-dimensional Reynolds-averaged compressible Navier-Stokes equations using mass-averaged variables[14] in strong conservation form.[15] Four different turbulence models are examined: Baldwin-Lomax,[16] Cebeci-Smith,[17] Jones-Launder[18] (k-ϵ) integrated to the wall, and Jones-Launder incorporating the Viegas-Rubesin wall functions[19] (see Table 2). For the Baldwin-Lomax model, three modifications were employed. First, the constant C_{cp} was modified[20] from the original value of 1.6 to 2.08. Second, the wake formulation for the outer eddy viscosity was not employed. Third, the location of the maximum in the outer function for the outer eddy viscosity was restricted to the region $n \le \delta_\infty$, where n is the distance normal to the surface, to avoid selection of spurious peaks outside the boundary layer. The Baldwin-Lomax model has been found to exhibit abrupt changes in the outer eddy viscosity length scale in two- and three-dimensional shock wave/turbulent boundary-layer interactions.[4,5,21] Similar behavior was observed herein for the swept compression corner. For the Cebeci-Smith model, the Van Driest damping factor $D = 1 - \exp(-nu_*/26\nu_w)$, where $u_* = \sqrt{\tau_w/\rho_w}$ is the local friction velocity, and ν_w is the kinematic viscosity at the wall. Also, the local edge of the boundary layer was determined by the smaller of the following: the height $y - y_{\text{surface}}$, where ρu reached a maximum, or the lowest height where $\Delta\rho u/\rho u \le 0.002$, where $\Delta\rho u$ is the difference in ρu between successive grid points. In all cases, the local edge of the boundary layer was never greater than $2\delta_\infty$. The reference velocity U_{ref} was defined as the velocity at the local edge of the boundary layer. For the Jones-Launder model, the constants $C_{\epsilon1}$ and $C_{\epsilon2}$ were modified to 1.44 and 1.92, respectively. The molecular dynamic viscosity is given by Sutherland's law.[22] The molecular and turbulent Prandtl numbers are 0.73 and 0.9, respectively.

The computational domain is shown in Fig 3. At the upstream boundary ABHG, which is parallel to the corner line FC, the incoming boundary layer was specified. Three cases (see Table 2) incorporated the variation of the upstream boundary-layer thickness on ABHG to precisely match the experiment. The remaining two cases employed a constant boundary-layer thickness on ABHG. Using a boundary-layer code on the flat plate upstream of the interaction, it was found that the variation of the incoming boundary-layer thickness δ_∞ along the upstream boundary ABHG was negligible. Therefore, the assumption of constant δ_∞ on ABHG does not affect the accuracy of the computed solutions.

Details of the computational grid are shown in Tables 3 and 4. Geometrically stretched grid systems were employed to insure accurate resolution of the flow features. Beginning at the corner line, the grid spacing in the x direction was stretched

Table 3 Details of the computational grid

Case	$\Delta x_{min}/\delta_\infty$	$\Delta x_{max}/\delta_\infty$	$\Delta y_{min}/\delta_\infty \times 10^3$	$\Delta y_{max}/\delta_\infty$	$\Delta z_{min}/\delta_\infty \times 10^2$	$\Delta z_{max}/\delta_\infty$	Δn^+, average
1	0.144	0.82	0.34	0.72	0.72	0.56	2.2
2	0.132	0.75	5.54	0.70	0.98	0.51	35.0
3	0.30	1.00	0.10	1.00	60.0	0.60	0.7
4	0.30	1.00	0.10	1.00	60.0	0.60	0.7
5	0.067	0.335	0.34	0.47	0.72	0.56	2.5

Table 4 Details of the computational grid

Case	N_x	N_y	N_z	Total points	t_{total}/t_c	Computer	CPU hours
1	64	46	40	117,760	4.1	CYBER 205	14.5
2	64	32	37	75,776	4.0	CRAY XMP	25.0
3	40	20	35	28,000	3.0	CRAY XMP	6.0
4	40	20	35	28,000	3.0	CRAY XMP	6.0
5	96	46	40	176,640	4.7	CYBER 205	12.8

typically by a factor of 1.02 in the upstream direction and a factor of 1.05–1.13 in the downstream direction. The grid spacing in the y direction was stretched by a factor of 1.2–1.3. Both stretched and uniform grid systems were employed in the z direction. A stretching factor of 1.2–1.3 was employed for cases 1, 2, and 5. Detailed comparison[9,10] indicated that a uniform grid system (as employed for cases 3 and 4) provided accurate resolution in the spanwise direction. All computations, except case 2, employed boundary conditions at the surface, and adequate resolution of the viscous sublayer was achieved (Table 3). In particular, the average value of the height (in wall units) $\Delta n^+ = \Delta n u_* / \nu_w$ of the first grid point adjacent to the surface satisfied $\Delta n^+ \leq 2.5$ for cases 1 and 5 (Baldwin-Lomax), and $\Delta n^+ = 0.7$ for cases 3 and 4 (Cebeci-Smith and Jones-Launder integrated to the wall).

An additional calculation was performed for the conditions of case 5 employing a larger grid spacing in the x and y directions, specifically, $\Delta x_{min}/\delta_\infty = 0.13$, $\Delta x_{max}/\delta_\infty = 0.61$, and $\Delta y_{max}/\delta_\infty = 0.70$. The results were found to be virtually identical to case 5 (e.g., the maximum change in surface pressure less than 3.5%), thereby confirming the accuracy of the computations.

The effect of the Reynolds number Re_{δ_∞} was investigated by a computation at $Re_{\delta_\infty} = 2.6\times10^5$ for $(\alpha, \lambda) = (24 \text{ deg}, 40 \text{ deg})$ using the Baldwin-Lomax model.[10] The comparison with experiment was similar to the cases presented herein at $Re_{\delta_\infty} \approx 9\times10^5$ and is therefore omitted.

The governing equations using the Cebeci-Smith and Jones-Launder models were solved using the hybrid explicit-implicit algorithm of MacCormack.[23] The equations using the Baldwin-Lomax model were solved using the hybrid explicit-implicit algorithm of Knight.[3] Both algorithms have been highly vectorized for execution on the CRAY XMP/YMP and CYBER 205 computers, respectively. (The hybrid algorithm of Knight has recently been vectorized for the CRAY YMP.) The governing equations were integrated in time from an assumed initial condition until a steady-state solution was achieved. The total physical time of integration t_{total} is shown in Table 4 in terms of the characteristic time t_c defined as the physical time required for a fluid particle to traverse the computational domain form the upstream to the downstream boundary in the inviscid region of the flow.

Comparison with Experiment

Surface Pressure

Experimental and computed surface pressure profiles for $(\alpha, \lambda) = (24 \text{ deg}, 60 \text{ deg})$ are shown in Fig. 4 at $z = 7.85\delta_\infty$. The ordinate is the dimensionless distance from the corner $(x - z \tan\lambda)/\delta_\infty$. The computed surface pressure profiles using both the Baldwin-Lomax and Jones-Launder models show general agreement with experiment. Except in the vicinity of the initial pressure rise (the upstream influence line), the calculated pressure is within 10% of the experiment. The underestimate of the upstream influence line has also been observed for the sharp fin.[3-5]

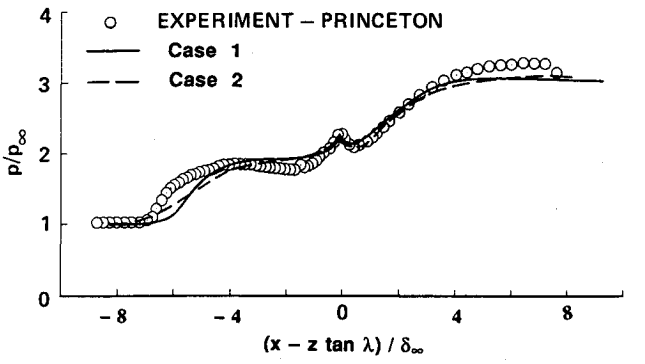

Fig. 4 Computed and experimental surface pressure for $(\alpha, \lambda) = (24 \text{ deg}, 60 \text{ deg})$.

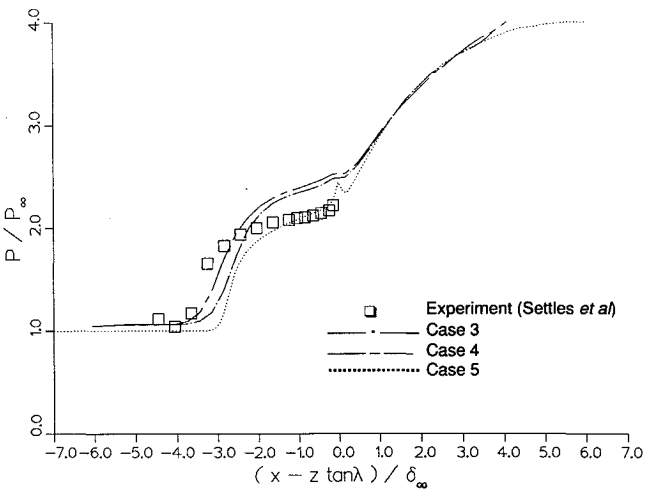

Fig. 5 Computed and experimental surface pressure for $(\alpha, \lambda) = (24 \text{ deg}, 40 \text{ deg})$.

Experimental and computed surface pressure profiles for $(\alpha, \lambda) = (24 \text{ deg}, 40 \text{ deg})$ are shown in Fig. 5 at $z = 10.0\delta_\infty$. General agreement is again observed between experiment and the computed profiles using the Baldwin-Lomax, Cebeci-Smith, and Jones-Launder models, although the experimental data are limited to points upstream of the corner line. Except in the vicinity of the upstream influence line, the calculated pressure for all cases is within 14% of the experiment. The Baldwin-Lomax model underestimates the upstream influence, but more accurately predicts the plateau pressure profile. The Cebeci-Smith and Jones-Launder models provide a more accurate prediction of the upstream influence, but overestimate the plateau pressure.

Flowfield Profiles

Experimental and computed boundary-layer profiles of pitot pressure p_p and yaw angle β are presented for the stronger interaction $(\alpha, \lambda) = (24 \text{ deg}, 40 \text{ deg})$. Detailed comparisons for $(\alpha, \lambda) = (24 \text{ deg}, 60 \text{ deg})$ are presented in Ref. 9 and show similar behavior.

Experimental and computed pitot pressure p_p, normalized by the upstream freestream pitot pressure p_{p_∞}, and yaw angle profiles for $(\alpha, \lambda) = (24 \text{ deg}, 40 \text{ deg})$ are shown in Figs. 6–8 and 9–11, respectively, at $z = 7\delta_\infty$. A total of 19 profiles each of pitot pressure and yaw angle were obtained in two separate investigations[8,10] at various x locations. (The experimental results of Refs. 8 and 10 are denoted as Settles et al. and Ketchum et al., respectively.) The three pitot pressure and yaw an-

gle profiles selected for presentation represent the essential features of the flowfield. The first profile ($x - z \tan \lambda = 0.4\delta_\infty$) is located near the corner line. The second profile ($x - z \tan \lambda = 2.6\delta_\infty$) is located near the line of divergence of the surface skin friction. The third profile ($x - z \tan \lambda = 6.0\delta_\infty$) is located far downstream of the corner interaction.

In Fig. 6, the experimental and computed pitot pressure profiles are displayed near the corner ($x - z \tan \lambda = 0.4\delta_\infty$). The Baldwin-Lomax model predicts the pitot pressure within 10%. Within the boundary layer, the Cebeci-Smith and Jones-Launder models underestimate the pitot pressure by as much as 30%; however, these models predict the peak pitot pressure within 2%. Outside the boundary layer, the computed profiles are diffused in the vicinity of the shock wave due to the shock-capturing nature of the numerical algorithms. In the vicinity of the line of attachment (Fig. 7), the computed pitot pressure profiles display excellent agreement with the experiment. All models predict the pitot pressure within the experimental uncertainty. Downstream of the interaction (Fig. 8), close agreement is again observed between the computation and experiment. Except in the immediate vicinity of the surface (i.e., within the lower 10% of the boundary layer), all models predict the pitot pressure within the experimental uncertainty.

In Fig. 9, the experimental and computed yaw angle β profiles are shown near the corner ($x - z \tan \lambda = 0.4\delta_\infty$). In the outer portion of the boundary layer, the computed profiles overestimate the yaw angle by as much as 20 deg; however, the predicted yaw angle near the surface agrees within 10%. In the vicinity of the line of attachment (Fig. 10) and downstream of the corner (Fig. 11), all models predict the yaw angle within the experimental uncertainty. Except in the immediate vicinity of the surface (i.e., within the lower 10% of the boundary layer) where the computed yaw angle profiles differ typically by 10%, the computed profiles are virtually identical, thereby indicating the insensitivity of the yaw angle to the turbulence model.

Flowfield Structure

The general agreement between the computations and experiment permits the determination of the flowfield model based on the computed resutls. The computed profiles of pitot pressure and yaw angle have been observed to be insensitive to the turbulence model employed, except within the immediate vicinity of the surface (e.g., the lower 10% or less of the boundary layer). It suffices, therefore, to examine the flowfield structure using the computed results of a single turbulence model (i.e., Baldwin-Lomax) with the understanding that some moderate quantitative differences exist between the different models near the surface.

The present paper describes the flowfield structure of the (α, λ) = (24 deg, 40 deg) and (24 deg, 60 deg) configurations using the computed flowfields obtained with the Baldwin-Lomax model. The computed skin-friction lines for the (α, λ) = (24 deg, 60 deg) configuration are shown in Fig. 12. The line of coalescence (line of separation in the sense of Lighthill[24]), formed by the convergence of upstream skin-friction lines, is clearly evident. As indicated by Lighthill,[24] "streamlines [in the vicinity of the surface] can increase greatly their distance from the surface...where skin-friction lines run very close together [i.e., at a line of coalescence]."

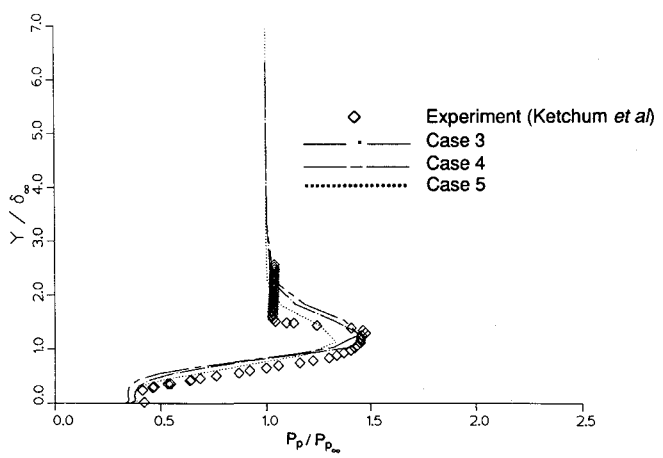

Fig. 6 Computed and experimental pitot pressure at $x - z \tan \lambda = 0.4\delta_\infty$ for (α, λ) = (24 deg, 40 deg).

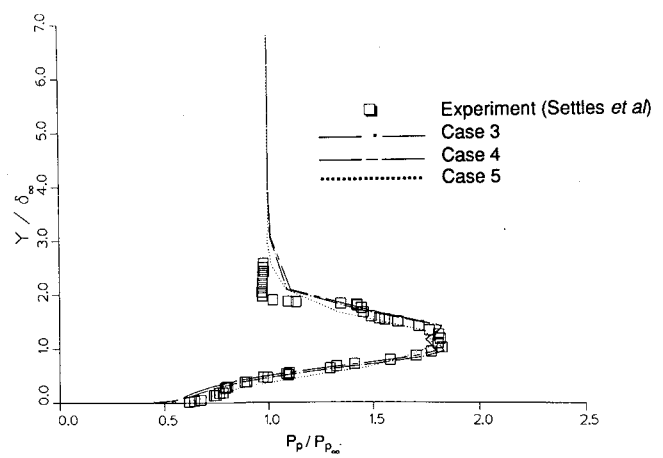

Fig. 7 Computed and experimental pitot pressure at $x - z \tan \lambda = 2.6\delta_\infty$ for (α, λ) = (24 deg, 40 deg).

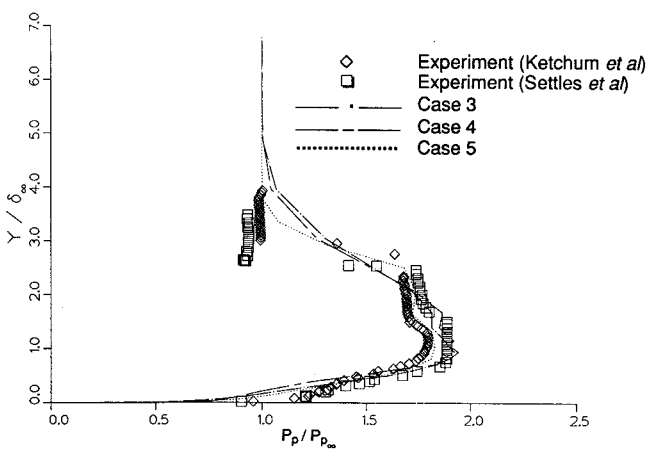

Fig. 8 Computed and experimental pitot pressure at $x - z \tan \lambda = 6.0\delta_\infty$ for (α, λ) = (24 deg, 40 deg).

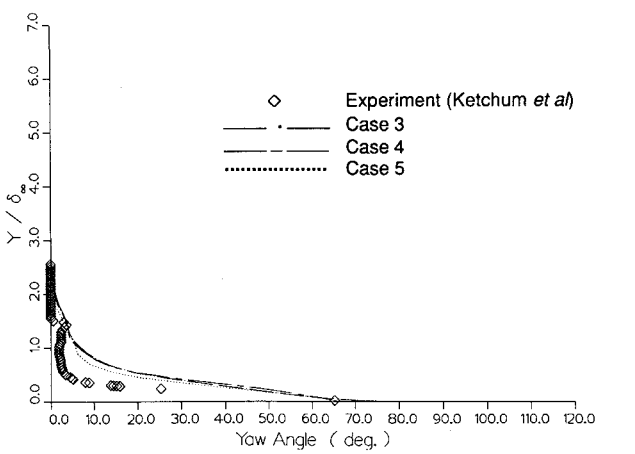

Fig. 9 Computed and experimental yaw angle at $x - z \tan \lambda = 0.4\delta_\infty$ for (α, λ) = (24 deg, 40 deg).

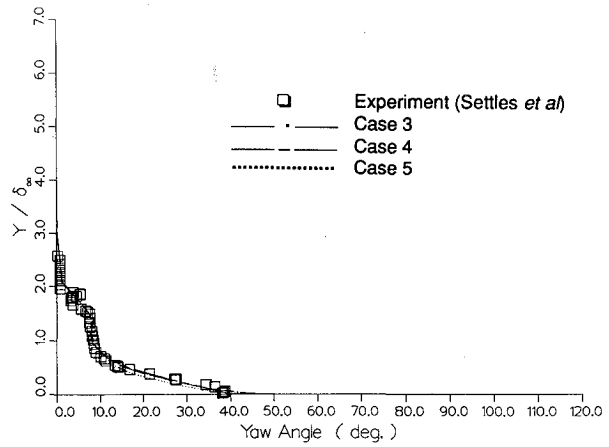

Fig. 10 Computed and experimental yaw angle at $x - z \tan \lambda = 2.6\delta_\infty$ for $(\alpha, \lambda) = (24 \text{ deg}, 40 \text{ deg})$.

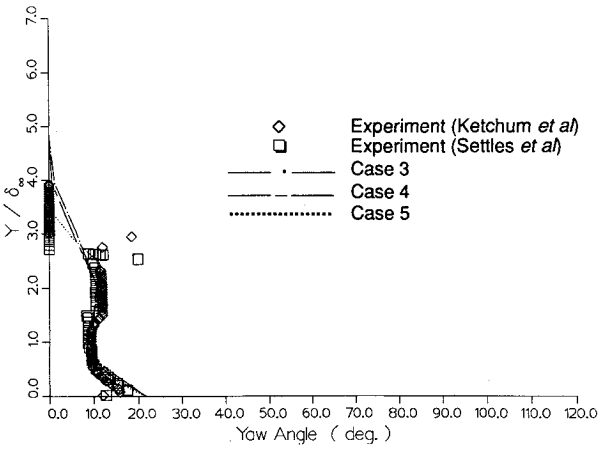

Fig. 11 Computed and experimental yaw angle at $x - z \tan \lambda = 6.0\delta_\infty$ for $(\alpha, \lambda) = (24 \text{ deg}, 40 \text{ deg})$.

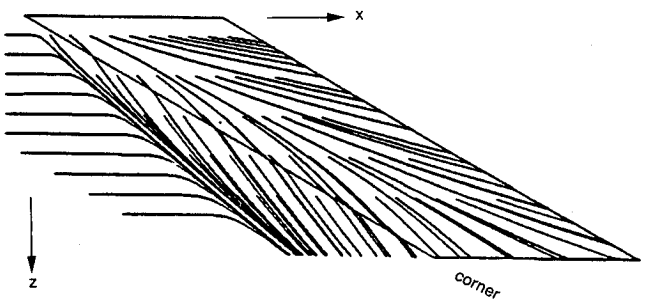

Fig. 12 Computed surface skin-friction lines for $(\alpha, \lambda) = (24 \text{ deg}, 60 \text{ deg})$.

The angle between the computed line of coalescence and spanwise coordinate z is approximately 10% greater than the experimental surface flow visualization.[10] Thus, the predicted extent of upstream influence is smaller than the experiment as observed in the surface pressure profiles. For the Jones-Launder model (with wall functions), the angle of the computed line of coalescence is approximately 5% greater than the experiment. The line of divergence (line of attachment) is situated on the compression surface.

Particle pathlines shown in Fig. 13 for $(\alpha, \lambda) = (24 \text{ deg}, 60 \text{ deg})$ depict the general streamline structure. The streamlines originate at two heights ($y = 0.2\delta_\infty$ and $0.8\delta_\infty$) along the upstream boundary of the computational domain ($x - z \tan \lambda = -12.2\delta_\infty$) and are spaced equally in the spanwise direction. The streamlines originating at $y = 0.2\delta_\infty$ form a vortical structure that is aligned with the corner. The sense of rotation is counterclockwise when viewed by an observer at the apex looking along the corner in the positive z direction. The streamlines originating at $y = 0.8\delta_\infty$ move over the vortical structure and continue downstream on the compression ramp. A similar structure is observed for the $(\alpha, \lambda) = (24 \text{ deg}, 40 \text{ deg})$ configuration.

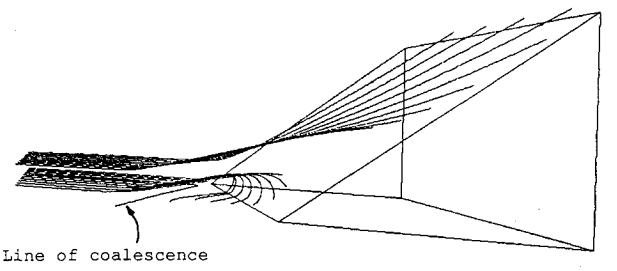

Fig. 13 Computed streamlines originating at $x - z \tan \lambda = -12.2\delta_\infty$ and $y/\delta_\infty = 0.2$ and 0.8 for $(\alpha,\lambda) = (24 \text{ deg}, 60 \text{ deg})$.

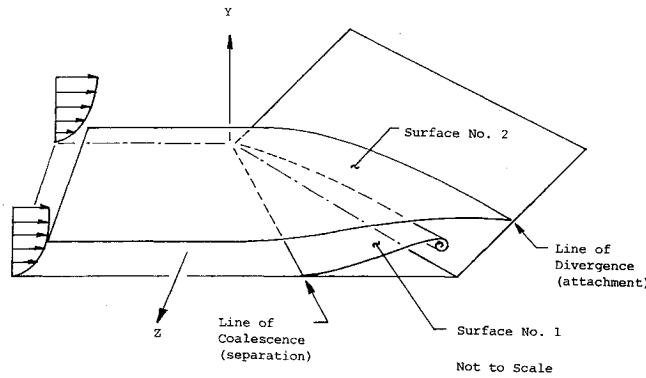

Fig. 14 Mean streamline model.

A general streamline model, developed on the basis of the results for the $(\alpha, \lambda) = (24 \text{ deg}, 40 \text{ deg})$ and (24 deg, 60 deg) cases, is presented in Fig. 14. It is noted that the model represents the mean streamline pattern. In the actual experiment, the flowfield is unsteady. The principal element is a large vortical structure. The line of coalescence defines a boundary of the three-dimensional surface of separation denoted as surface 1. This surface spirals into the core of the vortical structure. The flow in the vicinity of the surface exhibits a large yaw angle, and consequently, the streamlines are strongly skewed in the spanwise direction. The angle of intersection of surface 1 with the wall, measured in a plane orthogonal to the line of coalescence, was calculated to be approximately 10 deg for all cases examined. The line of divergence defines the intersection of a second surface, denoted as surface 2, with the swept compression ramp. This second surface extends upstream into the undisturbed flow. The fluid contained between the wall and surface 2 becomes the vortical structure. The fluid above surface 2 passes over the vortical structure and continues up the compression ramp. The general features of the streamline structure for the swept compression corner shown here are similar to the structure for the sharp fin.[5]

An important feature of surface 2 is its height above the wall, measured at a fixed x upstream of the interaction. The calculated height of surface 2 is displayed in Fig. 15 for the $(\alpha, \lambda) = (24 \text{ deg}, 40 \text{ deg})$ and (24 deg, 60 deg) cases. The height was determined by releasing fluid particles at various heights y/δ_∞ at a fixed upstream location and variable spanwise location z/δ_∞ and observing whether the particle pathline (streamline) moved up the compression surface or spiraled into the vortical structure. Two lines are shown in Fig. 15 for each case to represent the upper and lower estimates of the height of surface 2. The upper estimate indicates the maximum height y/δ_∞ of particles (at the spanwise location z/δ_∞), which were

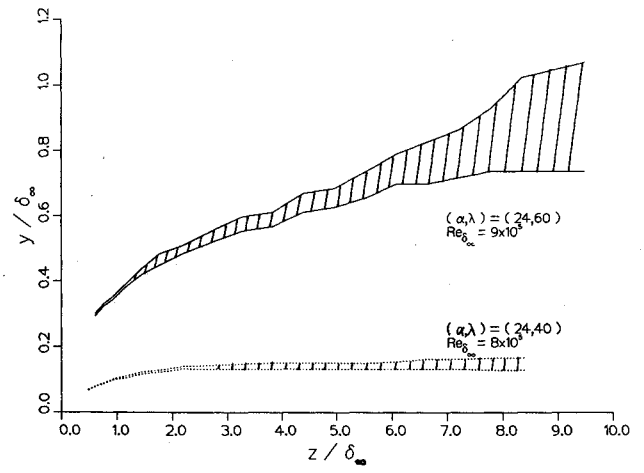

Fig. 15 Height of surface 2 for (α, λ) = (24 deg, 60 deg) and (24 deg, 40 deg).

observed not to pass over the vortical structure and continue up the compression ramp. The lower estimate indicates the maximum height of particles, which were observed not to enter the vortical structure. The uncertainty is attributable to the limited spanwise extent of the computational domain in which to view the pathlines, i.e., particles moving close to the line of attachment exited the computational domain before it was possible to determine whether they would become entrained into the vortical structure or pass overhead. Greater uncertainty arises at increased spanwise distance z/δ_∞ due to the decreased remaining spanwise extent of the computational domain in which to view the pathlines. It is important to note that the height for the (α, λ) = (24 deg, 40 deg) configuration appears to asymptote $y/\delta_\infty = 0.15$, whereas for the (α, λ) = (24 deg, 60 deg) configuration, the height continues to increase in an approximately linear manner. However, the limited spanwise extent of the computations precludes a definitive statement regarding the asymptotic behavior at large z.

A computational study of the contribution of inviscid and viscous effects on the evolution of the mean kinetic energy was performed.[9,25] The study suggests that the flowfield is predominantly inviscid and rotational throughout the boundary layer except within a narrow region adjacent to the surface and in an isolated region within the interaction near the corner. Further experimental and theoretical research is needed to clarify these issues.

Conclusions

A collaborative experimental and theoretical research program has focused on the three-dimensional shock wave/turbulent boundary-layer interaction generated by a three-dimensional swept-compression corner characterized by its streamwise compression angle α and sweepback angle λ. In the present study, computations have been performed for (α, λ) = (24 deg, 40 deg) and (24 deg, 60 deg) at Mach 3 and $Re_{\delta_\infty} \approx 9 \times 10^5$. The theoretical model is the three-dimensional Reynolds-averaged compressible Navier-Stokes equations with turbulence incorporated through a turbulent eddy viscosity. Four different turbulence models (Baldwin-Lomax, Cebeci-Smith, Jones-Launder with wall functions, and Jones-Launder integrated to the wall) have been examined.

The computed flowfields show overall good agreement with experiment. The surface pressure is predicted within 10 and 14% for (α, λ) = (24 deg, 60 deg) and (24 deg, 60 deg), respectively, except in the vicinity of the upstream influence line. The calculated pitot pressure profiles display close agreement with experiment for all turbulence models except at the corner where differences of up to 10% are noted for the Baldwin-Lomax model and up to 30% for the Cebeci-Smith and Jones-Launder models. Downstream of the corner, all models predict the pitot pressure within the experimental uncertainty except in the immediate vicinity of the surface (i.e., the lower 10% of the boundary layer). Likewise, the calculated yaw angle profiles display close agreement with experiment for all turbulence models except at the corner where differences of up to 20 deg are observed. Downstream of the corner, all models predict the yaw angle within the experimental uncertainty. Overall, the computed flowfields are insensitive to the turbulence model except in the immediate vicinity of the surface where differences of the order of 10% are observed in the pitot pressure and yaw angle.

The dominant feature of the three-dimensional swept-compression corner is a large vortical structure approximately aligned with the corner. A surface of streamlines, which is bounded by the line of separation (line of coalescence), forms the core of the vortical structure. A second surface originates upstream within the boundary layer and intersects the compression ramp at the line of attachment (line of divergence). The fluid contained between the wall and the second surface is entrained into the vortical structure. The height of this surface, measured immediately upstream of the interaction, is strongly dependent on the sweepback angle λ. The basic features of this flowfield are similar to the three-dimensional single fin.

A computational study of the inviscid and viscous effects on the evolution of the mean kinetic energy suggests that the flow is principally rotational and inviscid except in the immediate vicinity of the surface (where differences in predictions of the various turbulence models was observed) and in an isolated region within the interaction and near the corner. Further research is needed to clarify these issues.

Acknowledgments

This research was sponsored by the Air Force Office of Scientific Research under Grant 86-0266 and Contract F49620-86-C-0094 (monitored by James Wilson, Jim McMichael, and Len Sakell), NASA Ames Research Center, and the National Science Foundation. The computations were performed at the John von Neumann National Supercomputer Center and NASA Ames Research Center. The first author expresses his appreciation to Natraj Narayanswami for the analysis of the inviscid and viscous contributions to the mean energy equation, to Denise Raufer for the development of the streamline generation program, and to Dias Badekas for the preparation of the graphs.

References

[1]Settles, G., and Dolling, D., "Swept Shock Wave Boundary Layer Interactions," *Tactical Missile Aerodynamics*, edited by M. J. Hemsch and J. N. Nielsen, Vol. 104, Progress in Astronautics and Aeronautics, AIAA, New York, 1986, pp. 297–379.

[2]Settles, G., and Dolling, D., "Swept Shock/Boundary Layer Interactions—Tutorial and Update," AIAA Paper 90-0375, Jan. 1990.

[3]Knight, D., "A Hybrid Explicit-Implicit Numerical Algorithm for the Three-Dimensional Compressible Navier-Stokes Equations," *AIAA Journal*, Vol. 22, No. 8, 1984, pp. 1056–1061.

[4]Knight, D., "Calculation of Three-Dimensional Shock/Turbulent Boundary Layer Interaction Generated by a Sharp Fin," *AIAA Journal*, Vol. 23, No. 12, 1985, pp. 1885–1891.

[5]Knight, D., Horstman, C., Shapey, B., and Bogdonoff, S., "Structure of Supersonic Flow Past a Sharp Fin," *AIAA Journal*, Vol. 25, No. 10, 1987, pp. 1331–1337.

[6]Knight, D., Horstman, C. C., and Settles, G., "Three Dimensional Shock Wave Turbulent Boundary Layer Interactions Generated by a Sharp Fin at Mach 4," AIAA Paper 91-0648, Jan. 1991.

[7]Settles, G., and Teng, H.-Y., "Cylindrical and Conical Flow Regimes of Three-Dimensional Shock/Boundary Layer Interactions," *AIAA Journal*, Vol. 22, No. 2, 1984, pp. 194–200.

[8]Settles, G., Horstman, C. C., and McKenzie, T., "Experimental and Computational Study of a Swept Compression Corner Interaction Flowfield," *AIAA Journal*, Vol. 24, No. 5, 1986, pp. 744–752.

[9]Knight, D., Horstman, C. C., Ruderich, R., Mao, M.-F., and Bogdonoff, S., "Supersonic Turbulent Flow Past a 3-D Swept Com-

pression Corner at Mach 3," AIAA Paper 87-0551, Jan. 1987.

[10]Knight, D., Raufer, D., Horstman, C. C., Ketchum, A., and Bogdonoff, S., "Supersonic Turbulent Flow Past a 3-D Swept Compression Corner at Mach 3—Part II," AIAA Paper 88-0310, Jan. 1988.

[11]Settles, G., "An Experimental Study of Compressible Turbulent Boundary Layer Separation at High Reynolds Number," Ph.D. Dissertation, Dept. of Aerospace and Mechanical Engineering, Princeton Univ., Princeton, NJ, 1975.

[12]Settles, G., Perkins, J., and Bogdonoff, S., "Upstream Influence Scaling of 2D and 3D Shock/Turbulent Boundary Layer Interactions at Compression Corners," *AIAA Journal*, Vol. 20, No. 6, 1982, pp. 782–789.

[13]Sun, C.-C., and Childs, M., "Wall/Wake Velocity Profile for Compressible Nonadiabatic Flows," *AIAA Journal*, Vol. 14, No. 6, 1976, pp. 820–822.

[14]Rubesin, M., and Rose, W., "The Turbulent Mean-Flow, Reynolds-Stress and Heat-Flux Equations in Mass Averaged Dependent Variables," NASA TMX-62248, 1973.

[15]Pulliam, T., and Steger, J., "Implicit Finite-Difference Simulations of Three-Dimensional Compressible Flow," *AIAA Journal*, Vol. 18, No. 2, 1980, pp. 159–167.

[16]Baldwin, B., and Lomax, H., "Thin Layer Approximation and Algebraic Model for Separated Turbulent Flows," AIAA Paper 78-257, Jan. 1978.

[17]Cebeci, T., and Smith, A. M. O., *Analysis of Turbulent Boundary Layers*, Academic, New York, 1974.

[18]Jones, W., and Launder, B., "The Prediction of Laminarization with a Two-Equation Model of Turbulence," *International Journal of Heat and Mass Transfer*, Vol. 15, 1972, pp. 301–304.

[19]Viegas, J., Rubesin, M., and Horstman, C. C., "On the Use of Wall Functions as Boundary Conditions for Two-Dimensional Separated Compressible Flows," AIAA Paper 85-0180, Jan. 1985.

[20]York, B., and Knight, D., "Calculation of Two-Dimensional Turbulent Boundary Layers Using the Baldwin-Lomax Model," *AIAA Journal*, Vol. 23, No. 12, 1985, pp. 1849, 1850.

[21]Visbal, M., and Knight, D., "The Baldwin-Lomax Turbulent Model for Two-Dimensional Shock Wave/Boundary Layer Interactions," *AIAA Journal*, Vol. 22, No. 7, 1984, pp. 921–928.

[22]NASA Ames Research Staff, "Equations, Tables and Charts for Compressible Flow," National Advisory Committee for Aeronautics, Rept. 1135, 1953, Eq. A3, p. 19.

[23]MacCormack, R., "A Numerical Method for Solving the Equations of Viscous Compressible Flow," *AIAA Journal*, Vol. 20, No. 9, 1982, pp. 1275–1281.

[24]Lighthill, M., "Boundary Layer Theory," *Laminar Boundary Layers*, edited by L. Rosenhead, Oxford Univ., Oxford, England, 1963, pp. 72–82.

[25]Narayanswami, N., and Knight, D., "Viscous/Inviscid Effects in 3-D Shock-Wave Turbulent Boundary Layer Interactions," AIAA Paper 89-0358, Jan. 1989.